Nanoscale

Accepted Manuscript

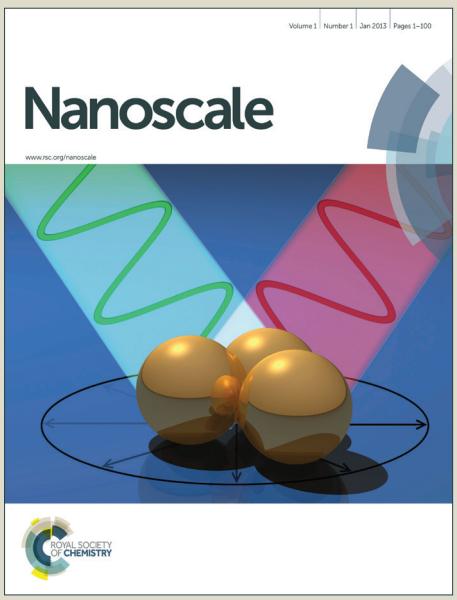

ROYAL SOCIETY OF CHEMISTRY

www.rsc.org/nanoscale

Molecular Release from Patterned Nanoporous Gold Thin Films

Ozge Kurtulus[1], Pallavi Daggumati[2], Erkin Seker[2*]

Departments of [1]Chemical Engineering and Materials Science and [2]Electrical and Computer Engineering, University of California, Davis, CA 95616, USA

*Corresponding author: eseker@ucdavis.edu

TABLE OF CONTENTS ENTRY

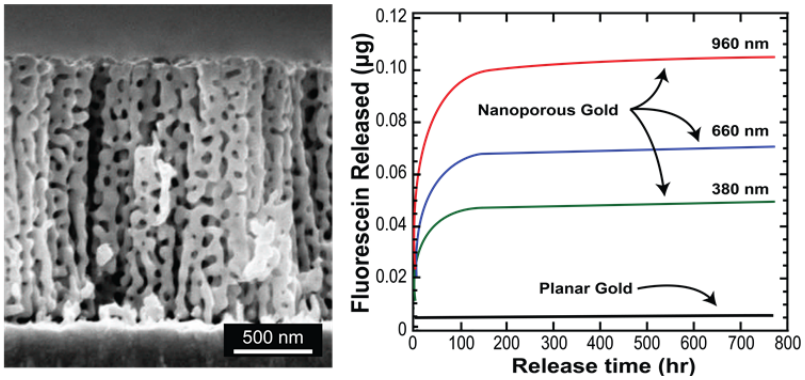

Patterned nanoporous gold thin films exhibit high loading capacity and tunable release kinetics for small molecules.

ABSTRACT

Nanostructured materials have shown significant potential for biomedical applications that require high loading capacity and controlled release of drugs. Nanoporous gold (np-Au), produced by an alloy corrosion process, is a promising novel material that benefits from compatibility with microfabrication, tunable pore morphology, electrical conductivity, well-established gold-thiol conjugate chemistry, and biocompatibility. While np-Au's non-biological applications are abundant, its performance in the biomedical field is nascent. In this work, we employ a combination of techniques including nanoporous thin film synthesis, quantitative electron microscopy, fluorospectrometry, and electrochemical surface characterization to study loading capacity and molecular release kinetics as a function of film properties and discuss underlying mechanisms. The sub-micron-thick sputter-coated nanoporous gold films provide small-molecule loading capacities up to 1.12 μg/cm^2 and molecular release half-lives between 3.6 hours to 12.8 hours. A systematic set of studies reveals that effective surface area of the np-Au thin films on glass substrates plays the largest role in determining loading capacity. The release kinetics on the other hand depends on a complex interplay of micro- and nano-scale morphological features.

INTRODUCTION

Biomedical devices, including drug-eluting cardiovascular stents and neural electrodes, have made a large impact on how diseases are treated[1-3]. Device coatings play a central role in the functionality of such devices and their interaction with the human body. Increasing demands on device features, such as reduced footprint, integration with electronics, controlled delivery of therapeutics, and minimal adverse tissue response,

require advancements on the coatings technology. Emergence of nanotechnology has spurred previously unattainable solutions to meet some of these challenges. One area that has greatly benefited from nanotechnology is drug delivery platforms. In these devices, a specialized coating responsible for drug delivery constitutes of a material architecture with sub-micron length-scales. Whether the coating is designed to biodegrade or maintain its structure over time, increased drug capacity contained within a small footprint and its controlled release are important figures of merit in either case. Nanostructured materials, including anodic nanoporous alumina[1], porous silicon[1, 4, 5], porous silica[6], porous carbon[7], carbon nanotubes[8-10], metal-oxide nanotubes[1, 9, 11], and porous polymers[12], have created tremendous advancements on this front. While there is an ever-expanding library of nanostructured materials[13], a remaining challenge has been their integration into miniaturized devices, as most of these materials have processing and synthesis conditions that are not fully compatible with conventional microfabrication techniques. In addition, for some biomedical devices, such as electrodes for electrophysiological recordings, it is also necessary for the material to exhibit high electrical conductivity as well as drug release performance and compatibility with standard micropatterning techniques. Nanoporous gold (np-Au) is an emerging material that has attracted significant interest with its high catalytic activity[14, 15], performance in optical and electrical biosensors/actuators[15-19], as well as a model system for nano-scale mechanical studies[19-21]. It is produced by dissolving silver from a silver-rich gold alloy by a process referred to as *dealloying*, where the combination of dissolution of silver atoms and surface diffusivity of gold atoms leads to a nanoporous metal. Some desired properties of np-Au include large surface area-to-volume ratio, well-established gold-thiol chemistry, electrical conductivity, and compatibility with conventional microfabrication processes (e.g., photolithography and physical vapor deposition). Its recent demonstrations in high-fidelity neural electrode coatings for electrophysiological recordings[3], biocompatibility[22-24], drug release performance to manage astrocytic proliferation[25], and non-biofouling features[26] highlight its potential as a novel multifunctional biomedical device coating. Here, we report a systematic study of film properties to determine loading capacity and molecular release kinetics by a combination of quantitative electron microscopy, fluorospectrometry, and electrochemical surface characterization. These results show a high loading capacity for small molecules and tunable release kinetics as a path to establishing np-Au as a novel drug delivery platform.

EXPERIMENTAL SECTION

Chemicals and materials

Thin (0.15 mm-thick) glass coverslips (12 mm × 24 mm), used as substrates for film deposition, were purchased from Electron Microscopy Sciences. Gold, silver, and chrome targets (99.95% pure) were obtained from Kurt J. Lesker. Polydimethylsiloxane (PDMS) sheets were obtained from B&J rubber products. Isopropyl alcohol, nitric acid (70%, used as received), fluorescein sodium salt and sodium hydroxide were purchased from Sigma-Aldrich. Sulfuric acid (96%) and hydrogen peroxide (30%) were obtained from J.T.Baker. Piranha solution, for cleaning glass coverslips, consisted of 1:4 ratio (by volume) of hydrogen peroxide and sulfuric acid. CAUTION: Piranha solution and nitric acid are highly corrosive and reactive with organic materials and must be handled with extreme care.

Sample preparation

Samples were prepared as described previously[27]. Briefly, the glass coverslips were cleaned by oxygen plasma exposure (Harrick Plasma Cleaner) for 40 seconds at 10 W and subsequent immersion in a freshly-prepared piranha solution for 10 minutes. The coverslips were then rinsed with deionized (DI) water and dried under nitrogen flow. PDMS stencil masks with millimeter-scale patterns were prepared using a laser cutter (VersaLaser, Universal Laser System)[28]. The patterns consisted of a 2 by 6 array of square openings (3 mm x 3 mm) that fit into each coverslip. The stencil masks were then cleaned with isopropyl alcohol and dried under nitrogen flow. Piranha-cleaned coverslips were aligned over the stencil with the sample surface facing the stencil. Samples were loaded into the sputtering machine (Kurt J. Lesker) for sequential deposition of metals. First, a 160 nm-thick chrome layer was sputtered at 300 W to promote adhesion between the glass substrate and the subsequent metallic layers. Next, 80 nm of gold was sputtered at 400 W as a seed layer to reinforce the porous coating. Finally, silver and gold were co-sputtered at 100 W and 200 W respectively. All depositions were performed under argon atmosphere at 10 mTorr. Different film thicknesses were obtained by varying the deposition time. At completion, each rectangular glass coverslip contained 12 identical metal patterns to be subsequently separated into individual glass chips (6 mm x 4 mm) for the release studies. Prior to dealloying the precursor AuAg alloy to produce np-Au films, the samples were treated with oxygen plasma for 40 s at 10 W and then dealloyed in nitric acid for 15 minutes at 55°C. Following dealloying, samples were rinsed with DI water three times and stored in DI water for at least a week while replacing the water every day. Before use, the samples were dried under nitrogen flow. In order to obtain samples with different pore morphologies, a group of dealloyed samples were thermally treated for 3 minutes at 200°C and 400°C in nitrogen atmosphere with a Heat Pulse rapid thermal annealer (Accu Thermo 610). The set of samples with different thicknesses and morphologies are referred to as sample set “T” and “M” respectively.

Morphological characterization of pores

Elemental compositions of the samples before and after dealloying were assessed with energy dispersive X-ray spectroscopy (Oxford INCA Energy-EDS). Top and cross-sectional views for each variety of samples were captured with scanning electron microscope (FEI Nova NanoSEM430) at 50 kX, 100 kX, and 150 kX magnifications to capture micro- and nano-scale morphological features, as well as thickness of np-Au films. Chrome and gold seed layer thicknesses were calculated using the previously calibrated deposition rates. The thicknesses of the deposited films were measured using a stylus-based profilometer (Dektak) and the alloy thickness (excluding the underlying chrome and gold layers) was determined by subtracting the calculated combined thickness of the underlying layers. The calculated alloy thicknesses were compared with the np-Au thicknesses obtained from the SEM cross-section images of the samples and the percent reduction in film thickness during dealloying was determined. Top-view images of samples were analyzed using ImageJ (National Institutes of Health shareware, http://rsb.info.nih.gov/ij/index.html) in order to determine the percent area covered by pores and cracks[27]. Briefly, the gray-scale SEM images were segmented into monochrome images in order to define pores and cracks as black and ligaments as white.

Electrochemical characterization of pore surface area

The effective surface areas of different samples were electrochemically determined, using a potentiostat (Gamry Reference 600) with a homemade Teflon electrochemical

cell, platinum counter electrode, and Ag/AgCl reference electrode. Cyclic voltammograms (CV) in 0.05 M sulfuric acid with a scan rate of 50 mV/s were obtained and the electrical charge under the gold oxide reduction peak between potentials of 720 mV and 970 mV was calculated. All calculated charge values were converted to the effective surface area by using 450 μC/cm^2 as specific charge of a gold surface[29, 30]. The ratio of the effective surface areas of different np-Au samples to the effective surface area of control planar-Au sample was defined as "enhancement factor".

Molecular release quantification

To test the performance of the samples in retaining and releasing drug molecules, fluorescein sodium was used as a small molecule drug surrogate, which is commonly used for its same order of magnitude molecular weight with that of small-molecule drugs[6, 31-34]. The samples (obtained by cutting the glass coverslips with metal patterns) with different film thicknesses and various pore morphologies were first oxygen plasma cleaned at 10 W for 40 s to increase the wettability of np-Au surface[27]. Samples were then placed in individual 0.2 mL PCR-tubes (USA Scientific) filled with 10 mM fluorescein sodium solution and incubated overnight at room temperature. After 16 hours, fluorescein solutions were aspirated and samples were rinsed three times with pipetted DI water and finally once in a beaker filled with 1 L of DI water to remove residual fluorescein from the samples. Following the rinsing step, the chips were transferred into fresh PCR tubes filled with 250 μL DI water as the elution medium. At specific time points, 10 μL of solution from the elution tube was sampled and mixed with 10 μL of 50 mM NaOH solution to enhance the fluorescence intensity[35]. Fluorescence intensities of the sampled solutions were measured at an emission wavelength of 515 nm with excitation wavelength of 470 nm using a fluorospectrometer (NanoDrop 3300).

Statistical Methods

Each study was performed on at least three different samples. Unless otherwise specified, the reported values represent averages (data points) and standard deviations (error bars and values following "±") of the measurements. Non-parametric Kruskal-Wallis test was used to identify differences between sample groups with different experimental conditions. When necessary, non-parametric Wilcoxon-Mann-Whitney (WMW) test was subsequently employed to conduct comparisons of two different sample groups. P-values less than 0.05 were deemed statistically significant. All p-values given in the text are for the Kruskal-Wallis tests unless otherwise specified.

RESULTS AND DISCUSSION

In this study, two sets of samples with systematically varying film thickness and pore morphology were fabricated and the corresponding drug loading capacity and release kinetics were investigated.

Sample Characterization

Three samples with different thicknesses (i.e., T1, T2 and T3) were produced from starting alloys with varying thicknesses (**Figure 1**). Sputter-deposition of samples allowed for precise control of film thickness by adjusting the sputtering time. Elemental composition of the co-sputtered alloy was 64.4±1.4 and 35.6±1.4, atomic percent of silver and gold respectively, as determined by EDS analysis of the samples. The small variation in elemental composition across the three samples (3-4% difference) shows precise control of alloy composition via the co-sputtering technique. Immersion of the alloy in concentrated nitric acid initiates the selective dissolution of silver and gold

surface diffusion at the acid-metal interface, resulting in the bicontinous open-pore structure displayed in **Figure 1**. After dealloying, final np-Au films typically had a residual silver content of 3-5%[15]. Unlike other nanoporous films with ordered pore morphology, such as anodic porous alumina[36, 37], np-Au exhibits a disordered porosity. The np-Au morphology is typically composed of features referred to as ligaments, pores, and cracks as described in **Figure S1**. Typical pore (dark regions in top-left insets in **Figure 1**) size was between 20-120 nm and the nanoporosity remained uniform through the film thickness (bottom images in **Figure 1**). The dealloying process may lead to film cracking (dark hairline regions prominent in top-right image insets in **Figure 1**). This is commonly attributed to volume contraction during dealloying[38], as well as the brittle nature of nanoporous metals and can be remedied by a variety of techniques, including optimization of the precursor alloy composition, dealloying conditions, and thermal treatment of the starting alloy[39-42]. SEM images reveal that varying film thickness had a negligible effect on film morphology. Although there were some crack formation in the thicker films due to the release of tensile stress in the film[41], all three different-thickness samples have similar morphology (p-value: 0.757 for the percent crack coverage comparison – see **Table S1**). This indicated that film thicknesses, at least in the sub-micron range, can be fabricated while having a minimal impact on the resultant pore morphology. This result, coupled with the ability to pattern the films via conventional microfabrication techniques, such as room temperature sputter-deposition, is a significant feature enabling integration of functional porous materials in miniature systems.

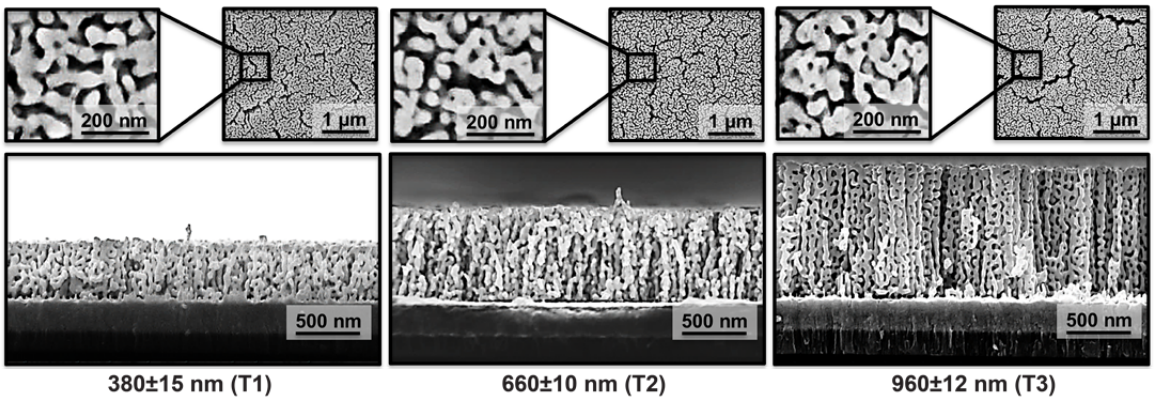

Figure 1: Scanning electron microscope images of cross-sectional (bottom) and top (at high and low magnifications in left and right insets, respectively) views of np-Au films with variable thicknesses yet similar morphology.

In order to investigate the effect of thin film morphology on release kinetics, we thermally treated a group of 960 nm-thick films (T3) and obtained various film morphologies (**Figure 2**). The thickest sample (T3) was selected for its highest loading/release capacity, therefore enhanced resolution in fluorospectrometric quantification of released fluorescein. The basis of morphology modification is that thermal treatment increases the surface diffusivity of gold atoms and coarsening of ligaments[40]. We have observed that the initial starting morphology had a significant effect on the morphology evolution as a function of thermal treatment. While np-Au thin films without cracks led to monotonous thickening of the ligaments and dilation of pores while preserving the characteristic morphological structure[43], in this study cracks in the starting film led to an 'islanding' phenomenon. That is, the islands with coalesced pores separated by augmented cracks appeared with increasing annealing temperature (**Figure 2**). The films treated at 200°C

(M2) displayed mild cracking and the films treated at 400°C exhibited significant sub-micron texturing. The statistical comparison of percent area coverage of the cracks observed in the SEM images of M1, M2, and M3, revealed a statistically significant difference (p-value: 0.018 – see **Table S1**). The pore coalescence and islanding phenomenon taken together are suspected to be responsible for the 12% and 17% decrease in the film thickness for M2 and M3 respectively in comparison to the untreated sample, M1 (see **Figure S3**). The observation of reduction in film thickness during dealloying and thermal treatment have been noted previously[38, 44].

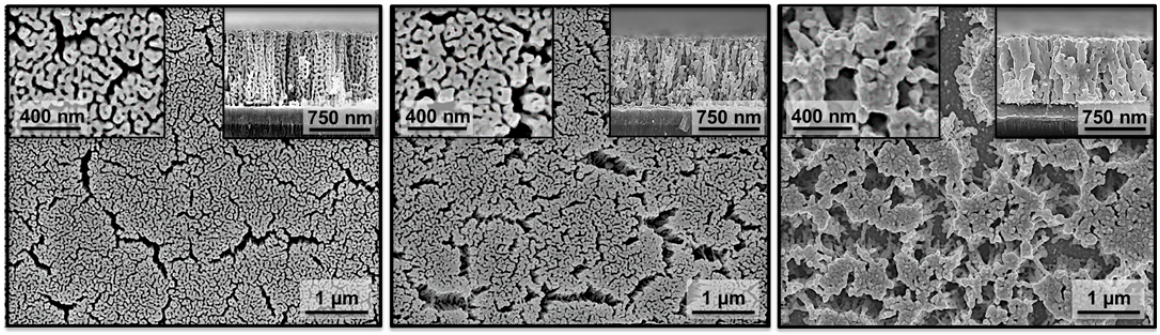

Figure 2: Scanning electron microscope images of top (main), magnified top (left inset), and cross-sectional (right inset) views of np-Au films treated at different temperatures to obtain various morphologies. Corresponding film thicknesses are included below the images.

Interfacial surface, that is, the solid surface that interacts with the fluid plays a crucial role in release kinetics and loading capacity[36, 37, 45]. For this reason, nanostructured materials with enhanced effective surface area (higher surface area-to-volume ratio) offer increasing loading capacity in small footprint. This is an important feature for miniature devices, such as implantable neural electrodes[46], where micropatterned nanostructured materials may still contain a physiologically-relevant amount of drug while having small form factor. The effective surface area, shown as “enhancement factor”, for each sample was calculated based on the charge included in AuO reduction, which was obtained by cyclic voltammetry measurements (**Figure 3**). As the AuO reduction only occurs at the gold surface interfacing the electrolyte, the measured current correlates with the effective surface area of np-Au. Electrical conductivity of the np-Au thin films allowed for electrochemical characterization of the surface area, where traditional surface area measurement techniques, such as BET, fall short as they typically require significantly more material in order to accurately quantify surface area. The obtained results were in agreement with BET studies of comparable sample morphologies of bulk np-Au used by different groups[30, 47]. The gain in surface area, referred to as enhancement factor, scaled linearly with thickness for films with uniform morphology (T1, T2, T3) (**Figure 3** inset). This suggested that the electrolyte had fully penetrated the porous network. Within the sample sets used for this study, thickest untreated film, T3 has the highest reduction peak which leads to the highest enhancement factor, 18.9. Thermal treatment reduced enhancement factor to 6.6 for the 400°C case plausibly via mechanisms such as pore coalescence (see **Figure S3**). Material characteristics obtained here were used for studying loading capacity and molecular release behavior.

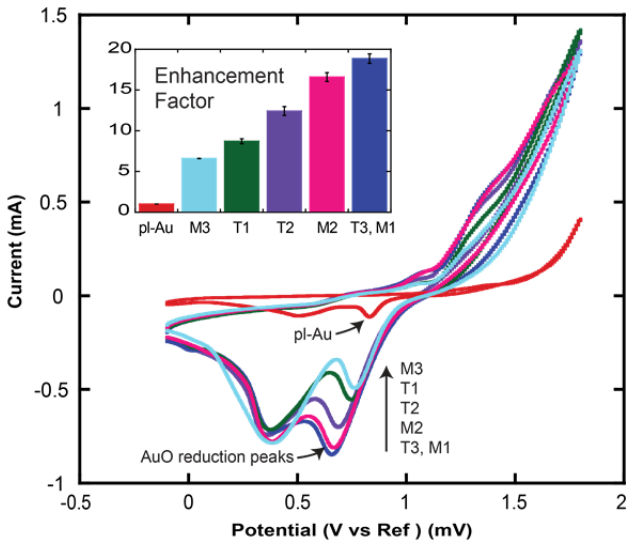

Figure 3: Cyclic voltammograms of T1, T2, T3 and M1, M2, M3 and corresponding surface area enhancement factors (inset). Orders of the stacked sample labels correspond to the order of Au reduction peaks.

Molecular release profile

In order to study loading capacity and molecular release kinetics for the np-Au thin film, all samples were loaded with fluorescein by immersing them in 10 mM fluorescein sodium salt dissolved in DI water. Preliminary studies indicated that steady-state loading isotherms were obtained in the range of 10 mM. The molecular release profiles for each sample, as shown in **Figure 4**, were analyzed to extract loading capacity and release kinetics. Each data point represents the average of six different chips and the error bars represent the standard deviation of these measurements.

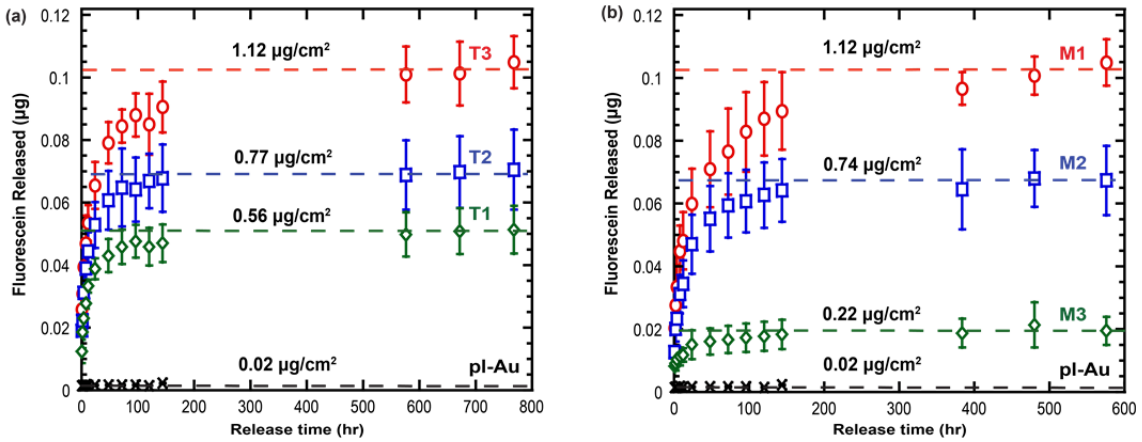

Figure 4. Mass of fluorescein released for (a) different film thicknesses and (b) different morphologies. Dashed lines indicate the averages of the steady-state points and corresponding loading capacities for each film.

Planar gold samples (pl-Au) did not retain or release a significant amount of fluorescein and produced a time-invariant release profile. This was attributed to the fluorescein load being limited to non-specifically adsorbed fluorescein molecules on the glass carrier substrate and the planar gold pattern on the glass coverslip. In both sets, np-Au chips released the fluorescein cargo for up to several weeks. The release profiles indicated

that the released amount monotonically decreased with decreasing thickness (**Figure 4a**) and increasing thermal treatment temperature (**Figure 4b**).

Loading capacity

Loading capacities of the different samples are presented as cumulative mass of fluorescein molecules released per unit footprint of the patterned film. The last three data points on the final plateau were averaged and divided by the footprint of the patterned films (3 mm x 3 mm) when the released fluorescein mass reached a steady-state. This calculated value represents the loading capacity for each film. We initially investigated loading capacity in relation to geometric film properties. The initial comparison was to check whether film thickness plays a global role in determining the loading capacity for np-Au gold films, with the minimal case being the planar gold film with zero porosity. **Figure 5a** shows that the loading capacity had a high correlation (R^2=0.99) with film thickness if the film morphology was similar between the samples, which is the case for the "T" sample set where statistical comparison of the film morphologies had not yielded a statistical difference (p-value: 0.119). This linear dependence also highlights that the films with different thicknesses were extremely similar in morphology and the entire thickness of the film was permeated with the fluorescein solution. On the other hand, the "M" sample set, consisting of annealed samples that exhibited reduction in film thickness upon thermal treatment, is weakly correlated with film thickness (R^2=0.60). The apparent change in morphology, including the predominant formation of cracks raised the possibility that majority of fluorescein should be stored within the porous regions of the film. For the case of M3, with cracks constituting a large portion of the film volume (see **Figure 2**), the remaining porous islands should account for the loading capacity. Indeed, molecular release from a highly fractal nanoporous network is likely hindered and/or dictated by other underlying mechanisms, leading to unusually long release durations that cannot be explained by classical Fickian diffusion in simple Euclidian geometries[48] (see discussion below). On the contrary, for close-to-micron scale unobstructed cracks, molecular release should largely be dictated by classical diffusion, for which a simple calculation of diffusion length, $x \approx \sqrt{(Dt)}$, suggests that the loaded fluorescein molecules should escape the cracks in approximately two milliseconds – a much shorter time than duration of the rinsing step. Given that the cracks constituted 23±2% of M3 samples in comparison to less than 6% for all other samples (**Table S1**), it is plausible that the reduction in capacity, despite the small change in thickness, should be accounted by the presence of cracks. Put another way, the loading capacity should scale with the volume of porous film. **Figure 5b** partially supports this hypothesis, as the capacity was highly correlated (R^2=0.99) with porous film volume for the "T" sample set with minimal cracking; although improved compared to that shown in **Figure 5a**, the correlation was still weak for the "M" sample set (R^2=0.75). This can be due to the porosity not being identical in the porous islands (cross-sectional view for M3, **Figure 2** and **Figure S3**) to that in the uncracked films. It is therefore necessary to take into account both micro- and nano-scale changes in morphology and thickness to fully describe the loading capacity. One way to do this is to use effective surface area (i.e., enhancement factor) as a descriptor of film morphology.

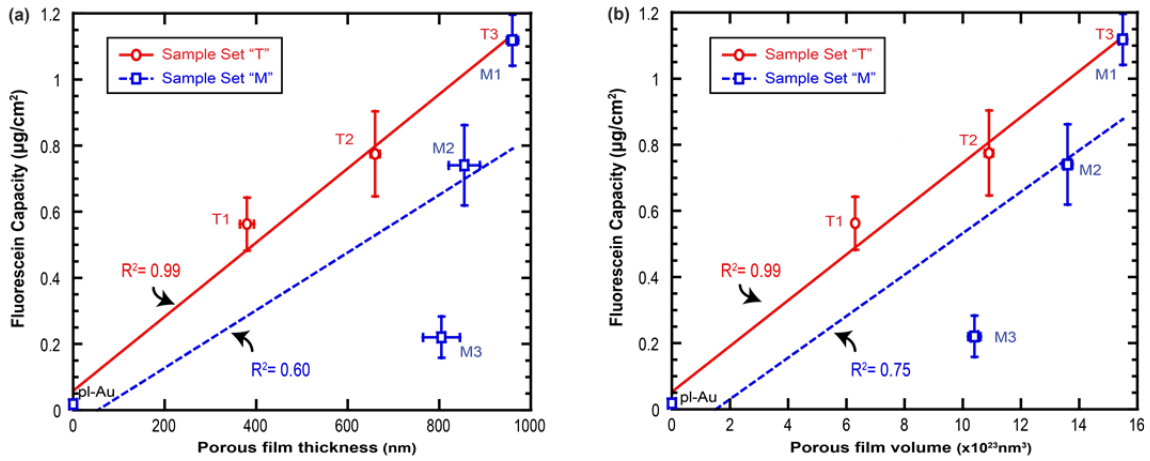

Figure 5. Loading capacity versus (a) film thickness and (b) porous film volume for different thicknesses (sample set "T") and morphologies (sample set "M").

Since effective surface area, as also stated elsewhere[37], plays a key role in nanostructured materials' performance in retaining molecules via surface adsorption, the enhancement factor could more accurately account for changes in nanoporosity, where the majority of the surface is packed with adsorbed molecules. The enhancement factor correlated linearly (R^2= 0.92) with the loading capacity of the entire set of samples used in this study, including all the different factors such as varying thicknesses and morphologies (**Figure 6**). This result also validates that the effective surface area plays an important role in molecular loading capacity in nanoporous thin films.

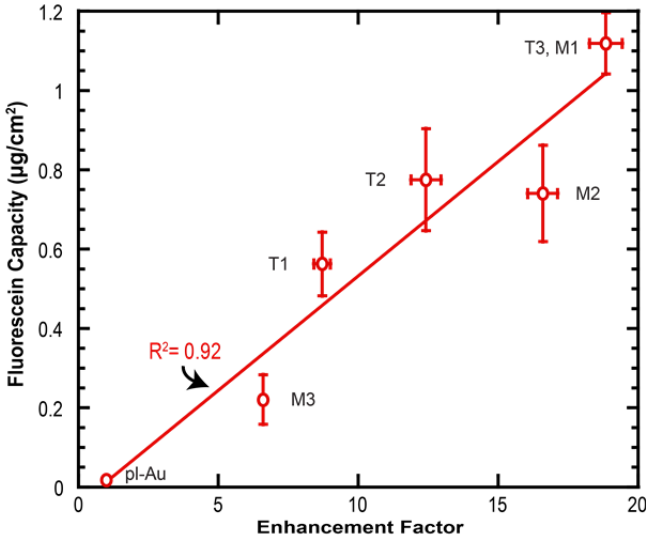

Figure 6. Loading capacity versus enhancement factor for all samples, including different thicknesses and morphologies, as well as planar gold controls.

In order to provide a deeper insight into the parameters that determine loading capacity in np-Au thin films patterned on glass substrates, we deconstructed the overall loading capacity into three components: (i) molecules contained in the pore volume; (ii) molecules absorbed over the porous surface, that is on the entire interfacial surface of the ligament network (**Figure S1**); and (iii) molecules non-specifically adsorbed on the glass carrier substrate and a planar gold pattern. **Figure 7** illustrates the contribution of

these factors in obtaining loading capacity (see **Table S2** for details), along with measured loading capacity, of nanoporous films with different thickness, yet with similar morphology (i.e., sample set "T").

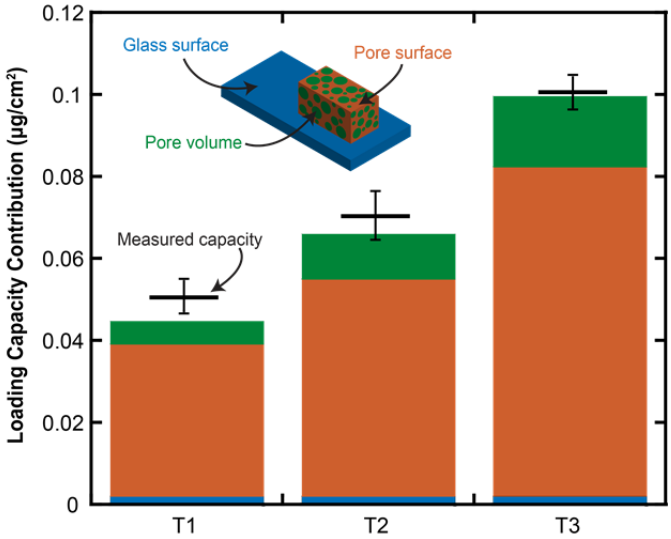

Figure 7: Calculated individual contributions of pore volume, pore surface area, and glass chip surface area (in the order of stacks in each column from top to bottom) to total calculated loading capacity along with the measured capacity values. The schematic represents the patterned np-Au on a glass coverslip. Thickness of the np-Au film in relation to the glass substrate is exaggerated for clarity.

The contribution of glass substrate and planar gold pattern was determined via release studies on the planar gold samples. All glass substrates were 6 mm by 4 mm and the gold pattern was 3 mm by 3 mm. The loading capacities of planar gold samples, obtained from the release profiles, were converted to mass of fluorescein to include in the overall contribution. This value, ~0.02 μg/cm^2, constituted 4.6%, 3.1% and 2.1% of the total loading capacities calculated for T1, T2 and T3 respectively. The premise of the contribution of fluorescein loaded into the pores is that the concentration of fluorescein within the porous network (excluding any adsorption onto the pore walls) should be equal to the loading solution concentration (10 mM) once equilibrium is reached. This concentration multiplied by the overall volume of the pores should approximate the amount of fluorescein stored in the porous thin film. The porous volume was estimated by multiplying the calculated volume of the film (modeled as a rectangular prism with measured dimensions of 3 mm x 3 mm x porous film thickness) with percent porosity (estimated to be ~55% by complete dissolution of silver from the an alloy of ~65% silver by atomic percentage and ~12% shrinkage of film during dealloying). These values, 0.006, 0.011 and 0.017 μg/cm^2, constituted 12.4% (T1), 16.7% (T2) and 17.3% (T3) of the total capacities calculated. The remaining percentage (83.0%, 80.2%, 80.6% for each film was hypothesized to be due to the adsorption of fluorescein molecules on the nanoporous surface. In order to calculate the effective surface area for each sample, we multiplied the surface area of planar gold (9 mm^2) with the enhancement factors obtained by the cyclic voltammetry experiments. Since the loading concentration of 10 mM led to steady-state isotherms, it is reasonable that the entire available surface was covered by approximately a monolayer of fluorescein atoms, which is 8.6 x 10^{13} molecules/cm^2 (1.4 x 10^{-10} mol/cm^2) in agreement with typical surface adsorbate densities published elsewhere[49]. The adsorbed fluorescein amount on the pore surface

was calculated by assuming fluorescein molecules as spheres packed in hexagonal arrangement with a packing density of 0.906[50]. Hydrodynamic radius of fluorescein molecules was calculated as 0.58 nm by Stokes-Einstein equation by taking diffusion coefficient of sodium fluorescein as 4.2 x10^{-6} cm^2/s in water at room temperature[51]. The theoretical study indicated that number of molecules adsorbed onto the surface had the most significant contribution to the overall loading capacity. The calculated loading capacities were 1.2% to 11.8% lower than the measured capacities, yet they still remarkably captured the possible underlying mechanisms of loading capacity (**Figure 7**). Some sources of this estimation error could be that hydrodynamic radius of fluorescein may decrease upon adsorption thereby increasing the number of molecules adsorbed onto the surface. The loading capacities obtained in this study were within the same order of magnitude with those obtained for other porous films, such as nanoporous carbon[7]. These results highlight the importance of surface area in loading capacity and the potential to tune loading capacity via surface modifications[37]. The electrical conductivity of the nanoporous gold films offers another unique opportunity to control the loading capacity of thin films[52]. It is possible to increase the loading capacity via applying an electrostatic potential to attract charged molecules onto the surface, thereby possibly reaching loading capacities that are not attainable in non-conducting porous thin films.

Release kinetics

Following the study on loading capacity of np-Au thin films, we investigated the effect of pore morphology on release kinetics. Normalizing the cumulative amount of molecules released by each sample type by their corresponding loading capacities allow for generating time-dependent fractional release curves (**Figure 8**). A consequent curve-fit analysis is then useful for providing insight into possible release mechanisms. **Figure 8** outlines the fractional release of fluorescein with respect to time for sample sets “T” and “M” respectively. The analysis of the release curves was performed by the semi-empirical power-law shown in Eq. (1)[53]:

$$\frac{M_t}{M_\infty} = kt^n \quad (1)$$

where M_t and M_∞ are cumulative amount of molecules released at a given time t and at the completion of release, k is the kinetic constant, and n is an exponent that describes the diffusional mechanism. If the exponent equals 0.5, then the molecular transport is deemed purely Fickian and if the exponent is 1, then the mechanism is thought to be Case II transport[53]. Application of the power-law to the current release studies produced exponent values that ranged between 0.14 to 0.24, which are outside the range described by the power-law model. One reason for this may be due to the highly disordered geometry of np-Au and high effective surface area-to-volume ratio may be leading to complex molecular release profiles. A complementary analysis method developed by Papadopoulou *et al.*, based on Monte Carlo simulation of diffusional molecular release in Euclidian (simple pore geometries) and fractal spaces captured the kinetics of tens of drug release experiments obtained from literature and computational studies for release from disordered matrices[48]. For this study, the authors employed the Weibull function (Eq. 2),

$$\frac{M_t}{M_\infty} = 1 - \exp(-at^b) \quad (2)$$

where *a* and *b* are constants, in which *b* was shown to serve as an accurate descriptor of possible release kinetics. Briefly, values of *b* between 0.69 and 1 were characteristic of molecular release from a normal Euclidian space, while values below 0.69 described geometries with increasing disorder with decreasing value of *b*. As shown in **Figure 8** insets, Weibull function fit the release data very well with the average R^2=0.99 for all sample types combined. The *b* values ranged from 0.43 to 0.56, with the exception of 0.32 for sample M3, which had the most disordered geometry including micron-scale cracks, and nanoporous islands of varying pore sizes (**Figure 2**). While further studies are necessary to fully extract the underlying mechanisms of molecular release from highly-disordered nanoporous gold thin films, the model predictions relating structural complexity of the film and release kinetics show good agreement.

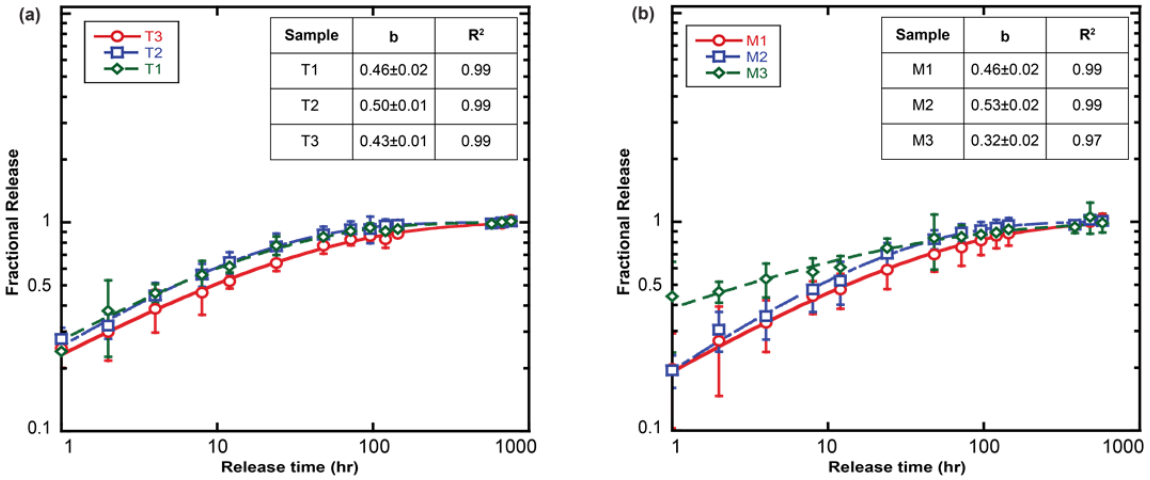

Figure 8. Fractional release profiles, for (a) different film thicknesses and (b) different morphologies, fitted to Weibull distribution function as a descriptor of putative release kinetics. The insets outline the resulting "b" value, used as the descriptor of release kinetics, along with the goodness of the fit.

In order to describe the effect of film morphology on release kinetics in a more applied fashion, we calculated half-lives for the different sample types, that is, the time it takes to release 50% of the loaded fluorescein capacity. Different thickness films with a similar morphology did not yield statistically different half-life (p-value: 0.164) with an average of 10 hours across all thicknesses, suggesting that the transport within the porous network, plausibly the region close to the film surface (where the molecules exit into the solution), dominantly determines the rate of release. For the purpose of putting the molecular release performance of np-Au in the context of other non-eroding porous coatings, here we outline the performance of several selected materials. It is important to emphasize that one should be careful in comparing molecular release performance of different platforms, since material nanostructure and surface chemistry, properties of the released molecules, and experimental conditions vary significantly between studies. Nanoporous anodized alumina (NAA) films with pore diameters (~100 nm) comparable to those of untreated np-Au exhibited release half-lives of approximately one hour for an anti-inflammatory drug molecule (indomethacin) with a comparable molecular weight to fluorescein used in our study[37]. One reason for increased half-life for molecular release from np-Au may be its highly-disordered porous structure in comparison to the ordered and columnar architecture of the porous alumina films. Indeed, porous silica films with more disordered pore geometry had release half-lives close to two hours for negatively-charged fluorescein isothiocyanate molecules[6]. In another study, the pore openings of

NAA films were reduced by plasma polymerization to less than 20 nm, which in turn extended release half-life to 100s of hours[54], supporting the significance of morphology on release kinetics and suggesting that the release half-life for np-Au thin films can be further enhanced by tuning pore diameters via additional gold deposition and/or polymerization.

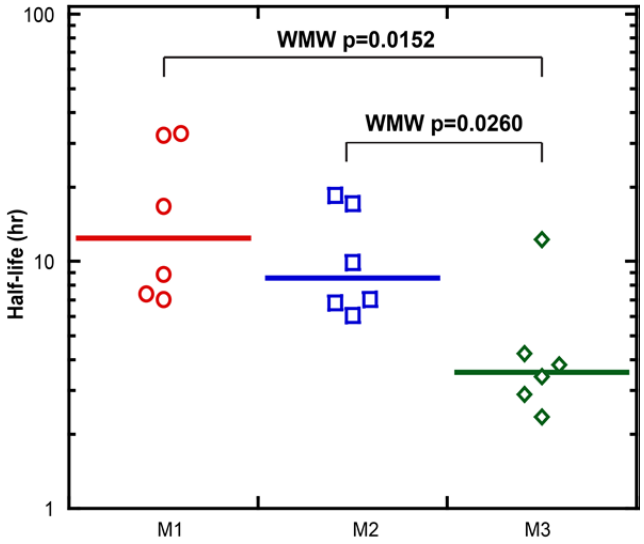

Figure 9. Half-life comparison for samples with different morphologies (M1, M2, M3). Solid lines indicate medians of the data points. Wilcoxon-Mann-Whitney (WMW) p-values show statistically-significant differences.

The sample set "M" with varying morphologies, exhibited distinct half-lives (**Figure 9**), with M3 releasing its content the fastest despite the lowest loading capacity. This, in part, suggests that the release rate is not strongly determined by the concentration gradient due to the amount of fluorescein inside and outside the film. We attributed the faster release from the M3 sample to cracks augmenting outer surfaces (revealed circumferential area of the islands in addition to their top surface) that created additional "flux surfaces" for molecules to exit the porous network (**Figure 2**), thereby increasing the rate of release. In order to test these hypotheses, we determined "flux surface area" for M1, M2, and M3 by analyzing the SEM images, with an assumption of similar pore morphology within the islands and the uncracked part of the films in order to simplify the model. The release half-life exponentially decreased with increasing flux surface area (R^2=0.96, see **Figure S2**). As seen in cross-sectional views (**Figure 2**), the porosity within the islands varies across the samples (**Figure S3**). It is therefore possible that both pore size and flux surface area play important roles in determining transport kinetics. It should be noted that the effective surface area decreases for sample set "M" with increasing annealing temperature due to pore coarsening and cracking, and the effective surface area is inversely proportional to the flux area. However, the absence of a correlation between effective surface area and flux surface area (and release half-life) for sample set "T" strengthen the argument that the release kinetics are largely dictated by the morphology for the np-Au thin films rather than the effective surface area. Coupled with tunable morphology of np-Au, the degree of control on release kinetics can be further enhanced by iontophoretic release of charged molecules enabled by np-Au's electrical conductivity[52]. This in turn should allow for highly tunable release kinetics across an extensive time range.

CONCLUSION

In this study, we demonstrated that the drug loading capacity and the release kinetics of nanoporous gold (np-Au) thin films can be tuned by modulating film thickness and morphology. We presented a systematic set of studies that revealed main physical mechanisms that dictated loading capacity and molecular release kinetics for nanoporous gold thin films. While loading capacity was largely determined by the effective surface area of thin films, the release kinetics depended on micro- and nano-scale morphological features of the thin films. We expect that these studies will assist future investigations on drug release from highly-disordered thin films and pave the way to integrating micro-patternable nanoporous gold thin films in miniature biomedical devices.

ACKNOWLEDGEMENT

We gratefully acknowledge the support from UC Lab Fees Research Program Award (12-LR-237197), Research Investments in the Sciences & Engineering (RISE) Award, and UC Davis College of Engineering start-up funds. We also thank Prof. Atul Parikh and Dr. Toros Çaglar for discussions on molecule-surface interactions and statistical analysis, Prof. Tingrui Pan for his help with stencil mask preparation, and Tatiana Dorofeeva for her assistance in obtaining scanning electron microscope images.

REFERENCES

1. E. Gultepe, D. Nagesha, S. Sridhar and M. Amiji, *Advanced drug delivery reviews*, 2010, **62**, 305-315.
2. V. S. Polikov, P. A. Tresco and W. M. Reichert, *Journal of neuroscience methods*, 2005, **148**, 1-18.
3. E. Seker, Y. Berdichevsky, M. Begley, M. Reed, K. Staley and M. Yarmush, *Nanotechnology*, 2010, **21**, 125504.
4. E. J. Anglin, L. Cheng, W. R. Freeman and M. J. Sailor, *Advanced drug delivery reviews*, 2008, **60**, 1266-1277.
5. L. Vaccari, D. Canton, N. Zaffaroni, R. Villa, M. Tormen and E. di Fabrizio, *Microelectronic engineering*, 2006, **83**, 1598-1601.
6. H.-Y. Lian, Y.-H. Liang, Y. Yamauchi and K. C.-W. Wu, *The Journal of Physical Chemistry C*, 2011, **115**, 6581-6590.
7. A. Labiano, M. Dai, D. Taylor, W.-S. Young, T. H. Epps III, K. Rege and B. D. Vogt, *Microporous Mesoporous Mater.*, 2012, **160**, 143-150.
8. A. Bianco, K. Kostarelos and M. Prato, *Current opinion in chemical biology*, 2005, **9**, 674-679.
9. M. Goldberg, R. Langer and X. Jia, *Journal of Biomaterials Science, Polymer Edition*, 2007, **18**, 241-268.
10. P. A. Tran, L. Zhang and T. J. Webster, *Advanced drug delivery reviews*, 2009, **61**, 1097-1114.
11. K. C. Popat, M. Eltgroth, T. J. LaTempa, C. A. Grimes and T. A. Desai, *Small*, 2007, **3**, 1878-1881.
12. D. A. Bernards, K. D. Lance, N. A. Ciaccio and T. A. Desai, *Nano Lett.*, 2012, **12**, 5355-5361.
13. G. Jeon, S. Y. Yang and J. K. Kim, *J. Mater. Chem.*, 2012, **22**, 14814-14834.
14. T. Fujita, P. Guan, K. McKenna, X. Lang, A. Hirata, L. Zhang, T. Tokunaga, S. Arai, Y. Yamamoto and N. Tanaka, *Nature materials*, 2012, **11**, 775-780.
15. E. Seker, M. L. Reed and M. R. Begley, *Materials*, 2009, **2**, 2188-2215.

16. G. M. Santos, F. Zhao, J. Zeng and W.-C. Shih, *Nanoscale*, 2014.
17. K. Hu, D. Lan, X. Li and S. Zhang, *Analytical chemistry*, 2008, **80**, 9124-9130.
18. J. Feng, W. Zhao, B. Su and J. Wu, *Biosensors and Bioelectronics*, 2011, **30**, 21-27.
19. H. J. Jin and J. Weissmüller, *Science*, 2011, **332**, 1179-1182.
20. A. M. Hodge, J. R. Hayes, J. A. Caro, J. Biener and A. V. Hamza, *Advanced Engineering Materials*, 2006, **8**, 853-857.
21. D. Lee, X. Wei, X. Chen, M. Zhao, S. C. Jun, J. Hone, E. G. Herbert, W. C. Oliver and J. W. Kysar, *Scripta materialia*, 2007, **56**, 437-440.
22. Q. Wei, Y. Zhao, C. Xu, D. Wu, Y. Cai, J. He, H. Li, B. Du and M. Yang, *Biosensors and Bioelectronics*, 2011, **26**, 3714-3718.
23. H. Qiu, Y. Sun, X. Huang and Y. Qu, *Colloids and Surfaces B: Biointerfaces*, 2010, **79**, 304-308.
24. Y. H. Tan, S. E. Terrill, G. S. Paranjape, K. J. Stine and M. R. Nichols, *Biomaterials Science*, 2014, **2**, 110-120.
25. E. Seker, Y. Berdichevsky, K. J. Staley and M. L. Yarmush, *Advanced Healthcare Materials*, 2012, **1**, 172–176.
26. J. Patel, L. Radhakrishnan, B. Zhao, B. Uppalapati, R. C. Daniels, K. R. Ward and M. M. Collinson, *Anal. Chem.*, 2013, **85**, 11610-11618.
27. P. Daggumati, O. Kurtulus, C. A. R. Chapman, D. Dimlioglu and E. Seker, *JoVE (Journal of Visualized Experiments)*, 2013, e50678-e50678.
28. A. Chen and T. Pan, *Biomicrofluidics*, 2011, **5**, 046505.
29. Y. H. Tan, J. A. Davis, K. Fujikawa, N. V. Ganesh, A. V. Demchenko and K. J. Stine, *Journal of materials chemistry*, 2012, **22**, 6733-6745.
30. E. Rouya, S. Cattarin, M. Reed, R. Kelly and G. Zangari, *J. Electrochem. Soc.*, 2012, **159**, K97-K102.
31. M. Chourasia and S. Jain, *Drug Delivery*, 2004, **11**, 129-148.
32. R. Pillai, D. Yeates, I. Miller and A. Hickey, *Journal of aerosol science*, 1994, **25**, 461-477.
33. Z. Liu, X. Sun, N. Nakayama-Ratchford and H. Dai, *ACS nano*, 2007, **1**, 50-56.
34. S. Giri, B. G. Trewyn, M. P. Stellmaker and V. S. Y. Lin, *Angew. Chem. Int. Ed.*, 2005, **44**, 5038-5044.
35. L. Huang, E. Seker, J. P. Landers, M. R. Begley and M. Utz, *Langmuir*, 2010, **26**, 11574-11580.
36. E. Gultepe, D. Nagesha, B. Casse, R. Banyal, T. Fitchorov, A. Karma, M. Amiji and S. Sridhar, *Small*, 2009, **6**, 213-216.
37. M. S. Aw, M. Kurian and D. Losic, *Biomaterials Science*, 2014, **2**, 10-34.
38. S. Parida, D. Kramer, C. Volkert, H. Rösner, J. Erlebacher and J. Weissmüller, *Phys. Rev. Lett.*, 2006, **97**, 35504-35506.
39. O. Okman, D. Lee and J. W. Kysar, *Scripta Mater.*, 2010, **63**, 1005-1008.
40. Y. Sun and T. Balk, *Scripta Mater.*, 2008, **58**, 727-730.
41. E. Seker, M. Reed and M. Begley, *Scripta Mater.*, 2009, **60**, 435-438.
42. N. Senior and R. Newman, *Nanotechnology*, 2006, **17**, 2311-2316.
43. Y. Ding, Y. Kim and J. Erlebacher, *Adv. Mater.*, 2004, **16**, 1897-1900.
44. E. Seker, J. Gaskins, H. Bart-Smith, J. Zhu, M. Reed, G. Zangari, R. Kelly and M. Begley, *Acta Mater.*, 2007, **55**, 4593-4602.
45. M. Napoli, J. Eijkel and S. Pennathur, *Lab on a Chip*, 2010, **10**, 957–985.
46. N. Kotov, J. Winter, I. Clements, E. Jan, B. Timko, S. Campidelli, S. Pathak, A. Mazzatenta, C. Lieber and M. Prato, *Adv. Mater.*, 2009, **21**, 3970-4004.
47. Y. H. Tan, J. R. Schallom, N. V. Ganesh, K. Fujikawa, A. V. Demchenko and K. J. Stine, *Nanoscale*, 2011, **3**, 3395-3407.

48. V. Papadopoulou, K. Kosmidis, M. Vlachou and P. Macheras, *Int. J. Pharm.*, 2006, **309**, 44-50.
49. J. B. Allen and R. F. Larry, *Department of Chemistry and Biochemistry University of Texas at Austin, John Wiley & Sons, Inc*, 2001.
50. H.-C. Chang and L.-C. Wang, *arXiv preprint arXiv:1009.4322*, 2010.
51. T. Casalini, M. Salvalaglio, G. Perale, M. Masi and C. Cavallotti, *The Journal of Physical Chemistry B*, 2011, **115**, 12896-12904.
52. S. Gittard, B. Pierson, C. Ha, C. Wu, R. Narayan and D. Robinson, *Biotechnology Journal*, 2010.
53. P. L. Ritger and N. A. Peppas, *J. Controlled Release*, 1987, **5**, 37-42.
54. S. Simovic, D. Losic and K. Vasilev, *Chem. Commun.*, 2010, **46**, 1317-1319.